The formation an destruction of Inversion Layers within a deep valley

Sandrine Anquetin, Claude Guilbaud, Jean-Pierre Chollet

The Formation and Destruction of Inversion Layers within a Deep Valley

SANDRINE ANQUETIN, CLAUDE GUILBAUD, AND JEAN-PIERRE CHOLLET

Laboratoire des Ecoulements Géophysiques et Industriels, UJF-CNRS-INPG, Grenoble, France

(Manuscript received 10 April 1997, in final form 2 March 1998)

ABSTRACT

The technique of large-eddy simulations has been used to investigate thermally driven local circulations in deep valleys for a complete diurnal cycle. A soil model simulates the thermal forcing at the ground, which depends on the season, the soil characteristics, the valley orientation, and the atmospheric variables.

The scales of interest are characteristic of an urban site located in a mountainous area, and the research focuses on low wind conditions without the influence of large-scale pressure gradients. This study highlights the influence of the season on the mechanisms responsible for the formation and the destruction of the thermal inversion layer. The spatial distribution of the convective boundary layer (CBL) within the valley is directly influenced by the season because of the variation of the solar warming. In summer, the altitude of the top of the CBL remains approximately constant across the valley, whereas in winter, this altitude varies with its location within the valley.

1. Introduction

Valleys produce their own local wind systems as a result of thermal differences. The most developed and most symmetric wind system might be anticipated in a deep, straight valley with a north–south axis. But even then, some asymmetry may develop with time due to the diurnal variation of the solar radiation input to west- and east-facing slopes. In the case of light geostrophic winds, upvalley and upslope winds usually form during the day due to surface heating. At night, surface cooling commonly leads to drainage flows in the reverse direction. In addition, with differential solar heating of the valley slopes, a cross-valley wind component may also develop.

While there are numerous studies dealing with the meteorology in wide valleys, there are relatively few studies of the dynamics of the atmosphere within narrow valleys. Furthermore, very little has been done toward understanding and/or modeling strong inversion conditions within these small valleys, despite the fact that the atmospheric dynamics within such a valley is often marked by a thermal inversion layer that reduces vertical exchanges between the bottom of the valley and larger atmospheric scales. For this atmospheric situation, the coldest (and densest) air settles to the lowest level and therefore potential temperature increases with height above the valley floor. Above this stably stratified part of the atmosphere, the so-called valley inversion, the normal adiabatic decrease of temperature with height, usually prevails (Oke 1987).

The formation and destruction of inversion layers are well described in the literature (Stull 1988), in which the time evolution of the inversion layer within a perfectly symmetric valley is usually presented. The physical mechanisms are qualitatively described without taking into account either the season that influences the solar radiation distribution or the valley orientation. From these descriptions, it is therefore difficult to obtain the characteristic timescale for the destruction–formation of an inversion layer.

A detailed paper from Whiteman (1982) introduces the timescale required for the destruction of the observed nocturnal inversion layer in deep mountain valleys in western Colorado. The observed vertical potential temperature profiles, at the center of the valley, evolve following one of three idealized patterns. The first pattern of inversion destruction is characterized by the upward growth from the ground of a convective boundary layer (CBL) and describes atmospheric boundary layer behavior over flat terrain. This occurred once on a summer day in the widest valley studied by Whiteman. The second pattern is an inversion destruction caused by the descent of the top of the inversion into the valley, which is accompanied by a warming of the valley atmosphere. This pattern was observed twice during field experiments in winter when the valley had extensive snow cover. The third pattern is a combination of the two previous ones and has been observed in all seasons. Inversion breakup is generally completed in 3–5 h after sunrise unless the valley is snow covered or the ground is wet.

Corresponding author address: Dr. Sandrine Anquetin, Laboratoire des Ecoulements, Géophysiques et Industriels, UJF-CNRS-INPG, BP 53 X, 38041 Grenoble, Cedex 09, France.
E-mail: Sandrine.Anquetin@hmg.inpg.fr

The inversion breakup was first simulated numerically by Bader and McKee (1983). The two-dimensional (2D) simulation was run taking into account two different time-dependent, analytic formulations for the heat flux at the ground. This study investigated the cross-valley evolution of the wind and temperature fields in an idealized east–west-oriented mountain valley. Their results showed that the heating distribution did not affect the evolution of the valley atmosphere. The redistribution of heat between slopes does not have a major influence. The atmospheric model did not tolerate large horizontal potential temperature gradients and reacted quickly to communicate disturbances through gravity wave interactions, probably due to the 2D approach of the study. Bader and McKee's subsequent paper (1985) presents the influence of several factors [e.g., width of the valley, initial nocturnal inversion layer (NIL) intensity within the valley, heat forcing, etc.] on the inversion breakup in the valley. The results of their 2D simulations are investigated in terms of time evolution of both the vertical structure of the NIL and the inversion layer intensity.

Various effects in the atmospheric boundary layer, such as those of vegetation, soils, turbulence, and clouds, were investigated using one-dimensional (1D) models by Garrett (1983) and Heilman and Dobosy (1985). These works showed that the drainage winds are sensitive to many external factors, such as ambient winds, cloud, and moderately dense forest canopy. Development of drainage winds apparently can be affected drastically by moderate changes in one or more of these factors. Nevertheless, these results need to be substantiated by three-dimensional (3D) models and specific field measurements.

Wong et al. (1987) presented a simulation of the nocturnal drainage winds in a small urban valley under strong inversion conditions ($R_i = 0.25$) with a 2D hydrostatic model. The thermal forcing, at the ground, is expressed using an analytical model of an experimental dataset. The four simulated hours are correctly predicted, leading to a 30% maximum discrepancy with the measured temperature profile.

In the early eighties, the Atmospheric Studies in Complex Terrain field experiment (Clements et al. 1989) was organized ''to improve fundamental knowledge of transport and diffusion processes on complex terrain, and to use this improved insight into the physics of terrain dominated flows to provide a methodology for performing air quality.'' Most of the published papers (special issues of *J. Appl. Meteor.*, **28,** issues 6 and 7) deal with the study of the driving forces, the structure, the dissipating effects, and the dispersion properties of locally driven cool-air drainage circulations in a valley.

The present work is dedicated to the simulation of the dynamics of a dry, low atmosphere—particularly the mechanisms of the formation and destruction of the inversion layers. In this study, the complete diurnal cycle in an idealized east–west-oriented deep valley is examined in order to characterize the dependency of the vertical extension of the inversion and its duration with the season. The forcing due to surface heating is obtained from the soil model, for which the only specified parameters are the type of soil and the time. A method is proposed for the determination of the characteristic length scales of the valley inversion (i.e., the top level of the CBL z_i and the top level of the inversion layer h_{st}). Therefore, by calculating these scales, the time evolution of the spatial structure of the inversion layer within the valley can be predicted.

The simulations are performed with the code Submeso that is under development within a national collaboration project. The code is based on the Advanced Regional Prediction System at the University of Oklahoma (ARPS 3.1) (CAPS 1993), a 3D nonhydrostatic model. Some new developments (Xue et al. 1995) performed at the Center for Analysis and Prediction of Storms since ARPS 3.1 have been included and modified for our own purposes. The numerical model, including the Navier–Stokes solver, the physical parameterizations such as the ground forcing through the soil model SM2-Isba, and the subgrid-scale turbulence, is described in section 2. Analysis and discussions are detailed in sections 3 and 4.

2. Model description

The Submeso model used in this work combines a large-eddy simulation of variable density flows with a soil model, SM2-Isba, which calculates the natural heat exchange between the ground and the air.

a. Submeso: An atmospheric model

As mentioned above, the dynamics of the inversion layer is directly linked to changes in buoyancy forces. It is thus necessary to go further than simulations using hydrostatic formulation of the equations and classic Boussinesq hypothesis to take into account more complete thermodynamics. In the atmospheric flows under consideration, where the velocity scale is small (i.e., a few meters per second) and the buoyancy is the main driving force, it may be important to consider temporal variation of density as well as density fluctuation in space to accurately compute the large-scale vertical acceleration.

1) THE SET OF EQUATIONS FOR THE LARGE-SCALE FLOW

The set of model equations is formulated to describe perturbations around an undisturbed, dry, hydrostatic base state that is a function of the altitude z only. Any variable Ψ is thus expressed as

$$\Psi(x, y, z, t) = \overline{\Psi}(z) + \Delta\Psi(x, y, z, t). \qquad (1)$$

The overbar is the temporally and horizontally invariant

base state and $\Delta\Psi$ is the deviation from this state. Furthermore, Ψ can also be expressed as

$$\Psi(x, y, z, t) = \langle\Psi(x, y, z, t)\rangle + \psi(x, y, z, t), \quad (2)$$

where $\langle\Psi\rangle$ denotes the large-scale field of the variable Ψ after the filtering operation using the grid mesh Δ_c as the characteristic length of the filter. The variable ψ represents the turbulent contribution that cannot be resolved explicitly. Nevertheless, it is involved in the mechanisms determining the evolution of large-scale fields through turbulent subgrid fluxes.

Momentum, continuity, and thermodynamic energy equations are used to compute the velocity U_i, the static pressure P, and the potential temperature Θ. In the following equations, c is the speed of sound, ν is the kinematic molecular viscosity, and R and C_p are, respectively, the universal gas constant and the specific heat at constant pressure. Here, f_i ($i = 1, 2, 3$) represents the Coriolis terms, and B_i stands for the buoyancy force.

The momentum equation is

$$\frac{\partial\langle U_i\rangle}{\partial t} + \langle U_j\rangle\frac{\partial\langle U_i\rangle}{\partial x_j} = -\frac{1}{\langle\rho\rangle}\frac{\partial\langle P\rangle}{\partial x_i} + \langle B_i\rangle + \langle f_i\rangle + \frac{\partial}{\partial x_j}\left[\nu\left(\frac{\partial\langle U_i\rangle}{\partial x_j} + \frac{\partial\langle U_j\rangle}{\partial x_i}\right) - \langle u_i u_j\rangle\right], \quad (3)$$

where U_i stands for the different velocity components: the west–east component U, the north–south component V, and the vertical component W. The pressure is chosen in preference to density as the prognostic variable, and density is derived from temperature and pressure. The pressure equation is obtained by taking the material derivative of the equation of state and replacing the time derivative of density by the velocity divergence using the mass continuity equation:

$$\frac{\partial\langle\Delta P\rangle}{\partial t} + \langle U_j\rangle\frac{\partial\langle P\rangle}{\partial x_j} = (\langle\rho\rangle c^2)\left(\frac{1}{\langle\Theta\rangle}\frac{\partial\langle\Theta\rangle}{\partial t} - \frac{\partial\langle U_i\rangle}{\partial x_i}\right). \quad (4)$$

The predictive form of the energy balance equation used here is

$$\frac{\partial\langle\Theta\rangle}{\partial t} + \langle U_j\rangle\frac{\partial\langle\Theta\rangle}{\partial x_j} = \frac{\partial}{\partial x_j}(-\langle\theta u_j\rangle). \quad (5)$$

The subgrid-scale turbulent fluxes (heat $\langle\theta u_j\rangle$, momentum $\langle u_i u_j\rangle$) must be expressed in terms of resolved-scale variables.

2) SUBGRID-SCALE TURBULENCE CLOSURE

As in any large-eddy simulation, small scales have to be modeled to estimate subgrid fluxes $\langle u_i u_j\rangle$ and $\langle\theta u_j\rangle$. These contributions are assumed to be proportional to the deformation and temperature gradient, respectively, through the subgrid-scale (SGS) eddy coefficients K_m and K_h for momentum and heat:

$$\langle u_i u_j\rangle = \frac{2}{3}e\delta_{ij} - K_m\left(\frac{\partial\langle U_i\rangle}{\partial x_j} + \frac{\partial\langle U_j\rangle}{\partial x_i}\right),$$

$$\langle\theta u_j\rangle = -K_h\frac{\partial\langle\Theta\rangle}{\partial x_j}. \quad (6)$$

In the atmosphere, even at the meso-γ scales under consideration, the filter width Δ_c is so wide (typically 100–200 m) that a large amount of turbulent fluctuations are associated with the unresolved scales. The unresolved SGS fluxes therefore have to be modeled carefully.

Another consideration, especially for the problem of inversions, is the effect of stratification that changes in space and time. It results in local and temporary reductions of turbulent fluxes along the vertical direction that has to be included in the SGS model. Also, the ground surface plays a major role in the dynamics under consideration. A significant amount of turbulence is produced in the vicinity of the ground, but it is not necessarily dissipated there.

For all these reasons, a transport equation based on the work of Moeng (1984) for SGS turbulent kinetic energy e is solved. For each type of stratification, a length scale l is determined. The equation for e is deduced from Deardorff (1980):

$$\frac{\partial e}{\partial t} + \langle U_j\rangle\frac{\partial e}{\partial x_j} = B_e - P_e + D_e - \varepsilon, \quad (7)$$

where the different terms of Eq. (7) are explicitly defined in Table 1.

TABLE 1. Modelization of the TKE equation terms.

SGS buoyancy production:	$B_e = K_h\langle\rho\rangle\frac{g}{\Theta_o}\frac{\partial\langle\Theta\rangle}{\partial z}$
SGS shear production:	$P_e = \langle\rho\rangle K_m S_{ij}^2 = \langle\rho\rangle K_m\left(\frac{\partial\langle U_i\rangle}{\partial x_j} + \frac{\partial\langle U_j\rangle}{\partial x_i} - \frac{2}{3}\frac{\partial\langle U_k\rangle}{\partial x_k}\delta_{ij}\right)^2$
Diffusion of e:	$D_e = \frac{\partial}{\partial x_j}\left(2K_m\frac{\partial e}{\partial x_j}\right)$
Dissipation rate of e:	$\varepsilon = C_e\frac{e^{3/2}}{l}$

The turbulent eddy viscosity K_m and the eddy diffusivity K_h are then expressed by

$$K_m = C_k l e^{1/2}; \qquad K_h = K_m(1 + 2l/\Delta_c). \quad (8)$$

For an unstable atmosphere, the mixing length is $l = \Delta_c$, where $\Delta_c = (\Delta_x\Delta_y\Delta_z)^{1/3}$, while in stable stratification, the mixing length is smaller than Δ_c and is assumed to be

$$l = 0.76e^{1/2}\left(\frac{g}{\Theta_o}\frac{\partial\Theta}{\partial z}\right)^{-1/2}. \quad (9)$$

Deardorff (1980) found that Eq. (9) gave good results in 3D simulations of the planetary boundary layer. Garrett (1983) also used an expression similar to Eq. (9) with good results for the prediction of drainage winds over an idealized constant slope.

3) Numerical resolution and boundary conditions

The governing equations are written in a curvilinear coordinate system, (ξ, η, ζ), with orthogonal directions ξ and η in the horizontal plane. The vertical grid is obtained by any vertical transformation specified by the user. The transformation Jacobians are calculated after the computational grid has been defined. In this present work, only the Gal-Chen and Somerville (1975) transformation is used.

Equations (3)–(5) are written in finite difference form on a staggered grid. In the late 1970s, along with the advancement of computer science and numerical computation techniques, nonhydrostatic models using compressible equations, where sound waves were not filtered out, were developed and put into pratical use. Tanguay et al. (1990) treated the terms related to sound waves semi-implicitly in both the vertical and horizontal directions, whereas Klemp and Wilhelmson (1978) used the so-called time splitting technique in which the sound waves are explicitly time integrated. The interest of this last approach is the explicit formulation of the pressure that avoids the inversion of a complex matrix at each time step. This technique may be implemented more easily on parallel or vector computers. Therefore, the equations are split into sound wave and gravity wave components, where the sound wave components are time integrated with a small time step ($\Delta\tau$), and the remaining terms are evaluated with a larger time step (Δt, where $\Delta t/\Delta\tau \simeq 10$). In a fully curvilinear coordinate system, this special handling of the sound wave terms reduces CPU time even with the severe constraint of the time step based on the sound wave velocity. Indeed, the Poisson equation, which diagnostically determines the pressure in the anelastic systems, has nonconstant coefficients (due to a stretched mesh or a coordinate transformation), and direct Poisson solvers are difficult to handle (Satomura 1989). The temporal discretization is carried out by the second-order leapfrog scheme with an Asselin (1972) time filter applied at every big time step.

The ground is the only physical boundary condition. Because of the major effect of the surface heat and momentum fluxes in the dynamics considered here, the next section is devoted to the presentation of the modeling of these fluxes.

b. SM2-Isba: A soil model for meso-γ scales

For our scales and configuration of interest, the soil–atmosphere interaction is the only forcing that has to be accurately reproduced. Variations in time and space of the heat and momentum fluxes at the ground are mainly responsible for the dynamics at local scales when the larger-scale forcing is not important. Indeed, the diurnal cycle of the solar radiation induces a timescale for changes in soil forcing, which imposes the temporal evolution of the atmospheric motion within the valley. The variation of inversion structure is also related to the diurnal cycle (Whiteman 1982).

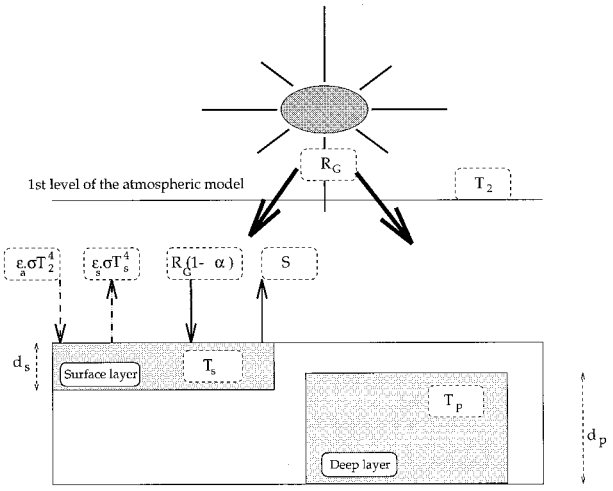

FIG. 1. Representation of the different terms of the energy budget in the SM2-Isba model.

The soil–vegetation model used in this study was developed specifically for use in mesoscale meteorology models. Based on the ISBA model (Noilhan and Planton 1989), the soil–vegetation model is designed to simulate the main processes involved in surface–atmosphere interaction with minimal complexity. It reproduces the exchanges among 1) a vegetation layer, 2) a thin surface layer (d_s = 10.0 cm) at temperature T_s, and 3) a deep layer (d_p = 1.0 m) at temperature T_p. The soil characteristics (conductivity, resistance) are associated with the thin surface layer, whereas the deep layer acts as a reservoir of energy. The soil–vegetation model includes prognostic equations for both soil temperature (T_s, T_p) and soil and vegetation moisture. Under the same wetness conditions of a same bare soil and under clear-sky anticyclonic conditions, the effect of latent heat flux with the season is hereafter neglected (Whiteman et al. 1996). This assumption would underestimate the total heat flux that would reduce the strength of convective motions that erode the inversion layer. Figure 1 simplifies the different terms of the energy budget at the surface. For a simulation with dry air, the driving term for the surface temperature T_s is the surface energy budget that includes the net radiation (R_n) and the sensible heat flux (S). The details of the land surface model can be found in Noilhan and Planton (1989). Our version of the model, SM2-Isba (Guilbaud 1996), was partially coded from the paper written by Noilhan and Planton. This model includes three parts.

1) A simple radiation model gives the radiative forcing to the soil model. The net solar flux (R_n) is the result of the radiation budget at the surface. The shortwave radiation is directly linked to the surface albedo α and the solar beam radiation at the ground R_G, whereas the longwave radiation is expressed by the two terms $\varepsilon_a \sigma T_2^4$ and $\varepsilon_s \sigma T_s^4$, where ε_a and ε_s are, respectively, the emissivity of the atmosphere and the surface; here, σ is the Stefan–Boltzmann constant ($\sigma = 5.67\ 10^{-8}$ W m^{-2} K^{-4}). Here, R_G depends on the latitude, the solar declination, and the slope of the surface. This simple model of radiation does not take into account either the integrated longwave radiation from all the atmospheric depth or the shade effect that might occur in the presence of any obstacle.
2) The soil model SM2-Isba gives the surface soil temperature T_s. Without the water cycle, the model is based on the equations for the temperature of the surface layer: $dT_s/dT = C_G(R_n - S) - (2\pi/\tau)(T_s - T_p)$ and the temperature of the deep layer: $dT_p/dT = (1/\tau)(T_s - T_p)$. Here, τ is the time constant, taken to be one day. The expression for C_G is given by Noilhan and Planton (1989). For a dry atmosphere, the expression is reduced to $C_G = C_{G,\text{sat}}$. Here, $C_{G,\text{sat}}$ is specificied through the 13 soil types of the Clapp–Hornberger classification (Clapp and Hornberger 1978). The SM2-Isba model successfully reproduces (Guilbaud 1996) the extensive field measurement data from the HAPEX-MOBILHY experiment (André et al. 1986).
3) Turbulent sensible heat and momentum fluxes are also in the surface layer model. The soil model output (surface temperature T_s) is connected to the atmospheric model Submeso by a wall model that calculates the surface heat and momentum fluxes. These fluxes are then introduced as SGS fluxes within the atmospheric model in Eqs. (3), (5), and (7). The wall model is based on the work of Louis (1979) for the stable case and of Byun (1990) for the unstable case. The bulk aerodynamic formulations of the heat and momentum fluxes introduce drag coefficients that depend on the stability of the atmosphere just above the ground and on the roughness length.

Therefore, the only data required in this model is the soil texture type. In the present version, the equations are integrated with a prediction–correction method using time step, Δt_{soil}.

c. Model evaluation

To evaluate the response of the Submeso code to real atmospheric flows, a 24-h evolution of an experimentally documented planetary boundary layer over a flat terrain is reproduced. Day 33 of the Wangara experiment is used because it has been already used as a reference for similar situations (Deardorff 1974; Yamada and Mellor 1975). The numerical simulation is initialized with the experimental data: the vertical profiles of temperature and velocity, the soil temperature, and humidity. The simulation is conducted for 10 h without any forcing apart from the geostrophic velocity. It was run on a 23 $\times$ 23 $\times$ 63 grid with $\Delta t = 2$ s and a resolution of $\Delta x = \Delta y = 150$ m and $\Delta z = 40$ m. Boundary conditions are periodic in the horizontal x and y directions. In Fig. 2, the height z_i of the CBL is plotted from the result of the simulation, the observations and the results of Deardorff's simulation (1974). The altitude z_i is determined by a method, detailed below, based on the analysis of the vertical heat flux profile. The model gives very good results especially during the growth of the CBL (between 0900 and 1200 LT). At the end of the growth of the CBL (at 1600 LT) the difference between the results obtained with Submeso and the observations is less than four vertical grid points.

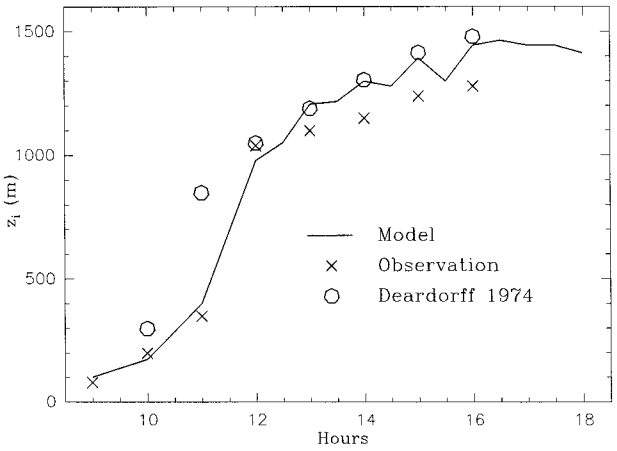

FIG. 2. Time evolution of the top level z_i of the CBL and comparison between the results from the simulation (solid line), the observations ($\times$), and the results from Deardorff ($\bigcirc$).

The combination of the soil model SM2-Isba with the wall laws properly models the heat and momentum exchanges at the ground boundary. Moreover, the SGS model acts very well in modeling the transport of the kinetic energy from the lower layers (close to the ground), where it is produced by solar warming and surface heterogeneity, toward the upper layers of the atmosphere (Guilbaud et al. 1997).

3. Three-dimensional stratified atmospheric flows within a valley

The structure of the boundary layer is investigated in a 3D schematic valley, where the depth is $H = 1260$ m and $L = 3000$ m is the width at the bottom. Figure 3 shows the whole domain of the simulation as well as the domain of visualization.

The valley topography is given by an analytical formula stemming from the classic Agnesi formula used in the simulations of stratified flow above single topography to investigate a range of length scales. The co-

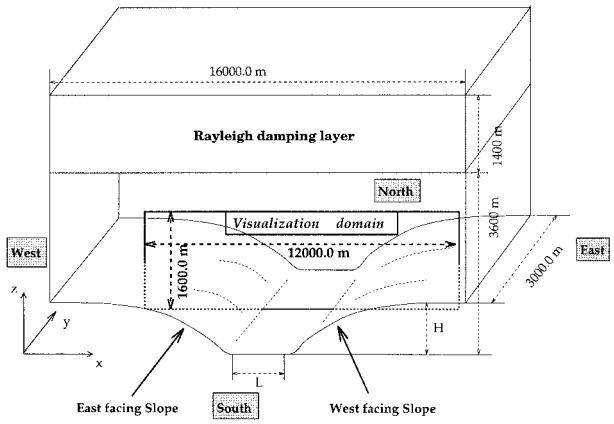

FIG. 3. Representation of the valley.

ordinate system does not allow slopes steeper than approximately 40°. The plateaus near the western and the eastern boundaries of the domain are used to restrict the effects of the lateral boundaries (radiative boundary type) in these directions. For northern and southern boundaries, periodic boundary conditions are prescribed to simulate a long valley. The ratio of the width of the bottom of the valley in the west–east direction to the depth of the valley ($L/H \simeq 2.4$) should allow several vertical structures to develop in the case of strong convective activity. At the top of the domain, we use a Rayleigh damping layer (Klemp and Lilly 1978).

Two simulations have been carried out to investigate the effects of the season on the mechanisms of the formation and destruction of the inversion layers. A typical day in winter (February) and a day in summer (August), at latitude 45°N and longitude 00°, have been considered. Due to the scales of interest, the Coriolis forcing $\langle f_i \rangle$ has been neglected Eq. (3). The numerical parameters are summarized in the Table 2.

The simulations were started 1 h after sunrise in summer and 1.5 h in winter. For both simulations, the temperature field is initialized with a constant stable stratification over the whole domain, characterized by the Brunt–Väisälä frequency (N) characteristic of the season. Therefore, no artificial vertical scale is introduced. The wind field is initially set to zero, which is consistent with the observed wind field early in the morning in a similar type of valley (Kuwagata and Kimura 1995). The air is assumed to remain dry.

The simulations are run for 48 h in both cases. This allows a balance of the heat exchange at the ground during the first 24 h and avoids any numerical dependency on the arbitrary initial conditions. Therefore, the results of the second day will be the only ones discussed below.

a. Solar heat forcing at the ground

The diurnal variation of the ground heat flux on the east- and west-facing slopes is plotted in Fig. 4 for the two seasons. This quantity is an output variable of the soil model SM2-Isba, and it has been averaged in the north–south direction. The east–west orientation of the slopes of the valley has been chosen to maximize the discrepancy of the solar radiation between the summer and winter (as already noted by Oke 1987).

We note that the nocturnal radiative cooling is almost the same for the two seasons due to the choice of the same type of soil. The absence of snow cover and any account of the water cycle causes the dry positive heat

TABLE 2. Numerical parameters of the simulations.

	Summer	Winter
Resolution $(nx)(ny)(nz)$	$83 \times 18 \times 53$	
$(\Delta n)(\Delta y)$ (m)	200×200	
Δz (m)	$75 \rightarrow 100$	
Time step Δt (s)	2	
Initial simulation time (LT)	0600	0800
Sunrise (SR)	0500	0630
Sunset (SS)	1845	1700
Soil type	Sandy–clay–loam	
Initial soil temperature (K)	273	263
Initial Brunt–Väisälä frequency (s^{-1})	1.9×10^{-2}	1.3×10^{-2}
Cray C98 CPU time	1680 s/simulated	

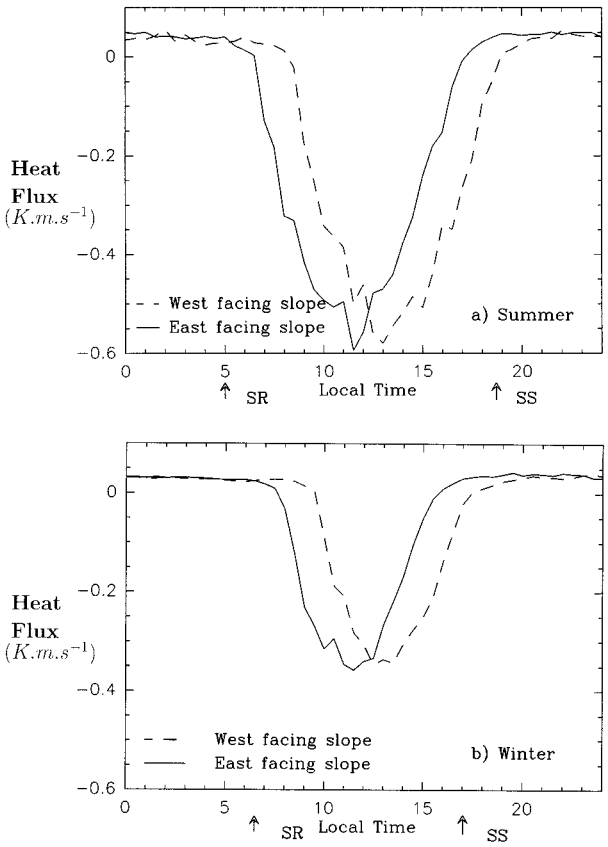

FIG. 4. Heat flux at the ground vs time. Here, SR refers to the sunrise and SS to the sunset.

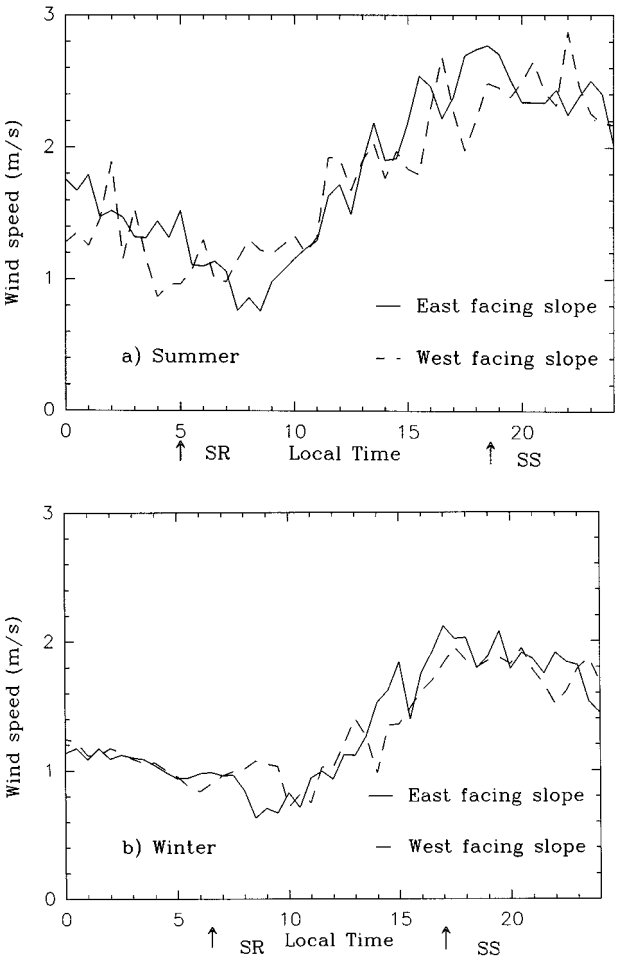

FIG. 5. Time evolution of the amplitude of the velocity at the ground.

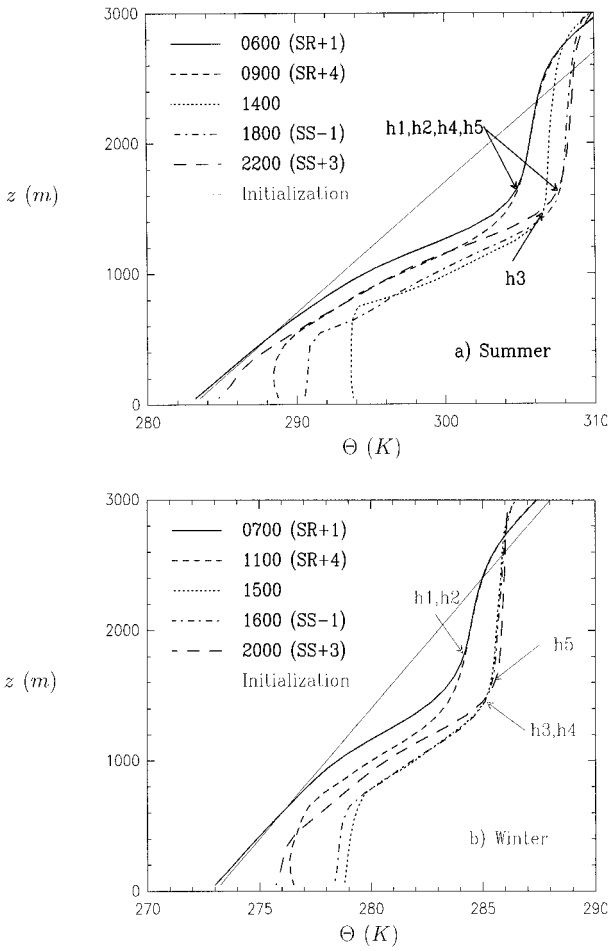

FIG. 6. Mean vertical profile of the potential temperature within the valley for different times.

flux to be essentially a function of the soil type and the wind field at the ground, which does not change significantly from one season to the other; see Fig. 5 ($\|\mathbf{V}\| \cong 1$ m s^{-1}). Nevertheless, we observe in Fig. 4 a serious discrepancy between the two maxima of the simulated heat flux observed around 1200 LT. This discrepancy is obviously linked to the amount of net solar radiation, which is stronger in summer.

The atmospheric flow is only generated by the thermal ground forcing since no other large-scale forcing is prescribed. This tends to reproduce the generation of local winds within a deep valley during a stable anticyclonic episode.

b. Dynamics of the atmosphere within the valley

The simulation provides values of pressure, velocity, density, and temperature at each time step and at each spatial location. These fields are analyzed by plotting isovalues of the variables (e.g., temperature) at given time steps. Such flow pictures help us to understand how the process evolves, particularly with time, and also how phenomena are distributed in space. To get results of general interest, the analysis needs some statistics that tend to damp the variability of the phenomena.

In Fig. 6, the vertical profiles of the potential temperature have been obtained by averaging the instantaneous profiles across the valley and in the north–south direction. In Fig. 6a, the NIL (solid line) is destroyed after sunrise by the upward growth from the ground of a warming CBL; the top of the inversion layer remains approximately constant (referred to as *h*). On the contrary, in Fig. 6b, in winter, the growth of the CBL is stopped once the CBL has attained a depth of 550 m. The inversion is then destroyed as the top of the NIL descends into the valley. This type of inversion subsidence has also been observed by Whiteman (1982) in winter.

Furthermore, in Figs. 7–11 we present vertical cross sections (referred to as visualization domain in Fig. 3) of instantaneous velocity vectors at each grid point superimposed on isolines of the instantaneous potential temperature. The times selected for presentation of these

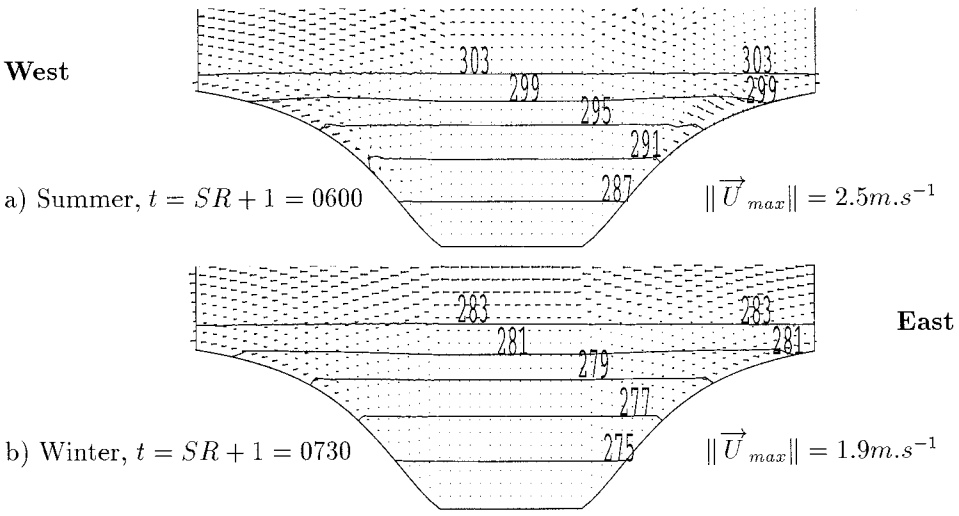

FIG. 7. Vertical cross section of the isovalue of the potential temperature Θ and the velocity vectors.

figures have been selected to show every important stage of the process during the day.

1) DAWN

In Fig. 7 the NIL within the valley and above the plateaus is characterized by low wind speed (less than 2.5 m s^{-1} in summer and 1.9 m s^{-1} in winter). The temperature isolines are horizontal. The intensity of the stratification in the valley is stronger in summer ($N = 2 \times 10^{-2}$ s^{-1}) than in winter ($N = 1.5 \times 10^{-2}$ s^{-1}). The noctural flow during the night fills the valley with cold air, and the stratification gets stronger since soil and air temperature balance each other. Thus, the velocities are considerably reduced in the lower part of the valley. The flow in the upper part of the valley and along the plateaus remains unchanged from the previous day.

2) MORNING

The anabatic wind develops along the sunny east-facing slope and leads to the destruction of the inversion above this slope (see Fig. 8). This atmospheric motion impacts on the inversion lid, generating, therefore, two counterrotating vortices within the valley. Due to the valley orientation, this motion is asymmetric with a stronger vortex on the east-facing slope at this time of the day. Therefore, an intense vertical motion develops in the western part of the valley.

3) MIDDAY

In Fig. 9 the inversion above the plateaus has been completely destroyed by convective upward velocity due to the ground warming. The upward motion within

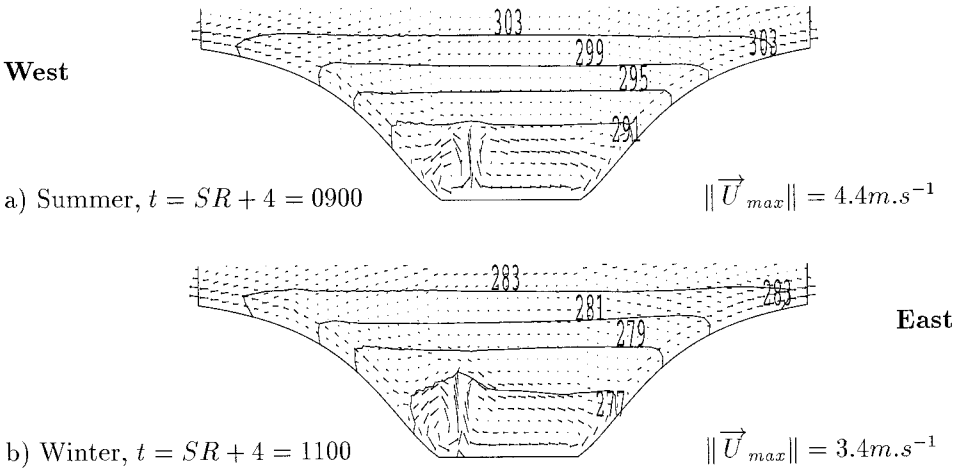

FIG. 8. Vertical cross section of the isovalue of the potential temperature Θ and the velocity vectors.

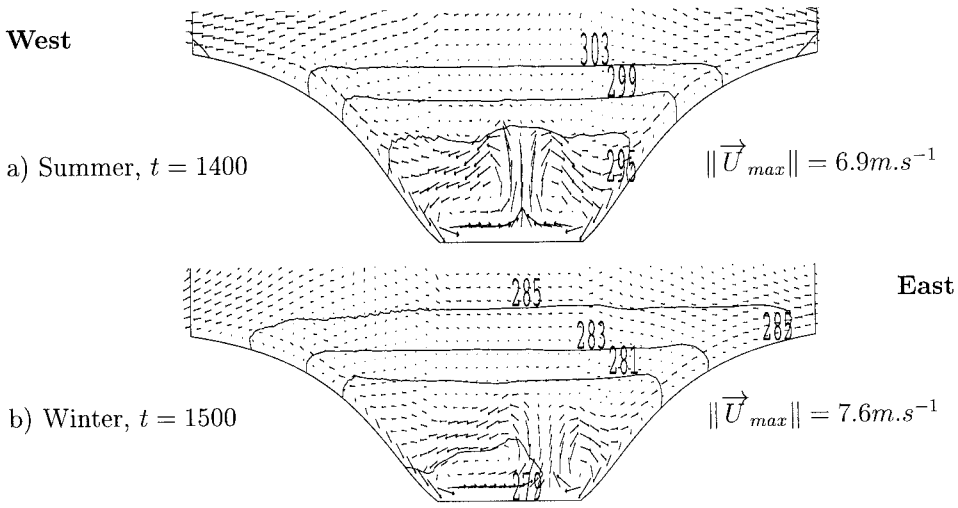

FIG. 9. Vertical cross section of the isovalue of the potential temperature Θ and the velocity vectors.

the valley has moved from the west side toward the east side of the valley. For both seasons, a stably stratified layer persists in the upper part of the valley. Due to mixing in lower layers, the temperature is homogeneous close to the ground. The large-scale motion above the inversion is due to the warming of the plateaus. Nevertheless, in summer, the isolines of the potential temperature remain horizontal, leading to a well-mixed atmosphere under the inversion lid. In contrast, in winter, the structure of the temperature field is more complex. Therefore, the flow is accelerated within a thinner layer near the ground than in summer, leading to a higher maximum velocity.

4) EVENING

There is an asymmetrical damping of the velocity within the valley due to the radiative effect along the west-facing slope (see Fig. 10). The two counterrotating vortices are less energetic but still active in the bottom of the valley, creating a well-mixed atmospheric layer. In the summer case (Fig. 10a), the longwave radiative cooling of the ground starts to create a new inversion. The motion in and above the valley has decreased (≈5 m s^{-1}) and its vertical extent is reduced (cf. the one at 1400 LT). In winter, the vertical extent of the motion within the valley is larger and the velocity intensity is almost the same as in summer. A vertical motion develops along the west-facing slope (the last sunny slope).

5) NIGHTFALL

The katabatic wind develops along both slopes (see Fig. 11). The central core of the valley is cooled down, and a new inversion is created. The intensity of the

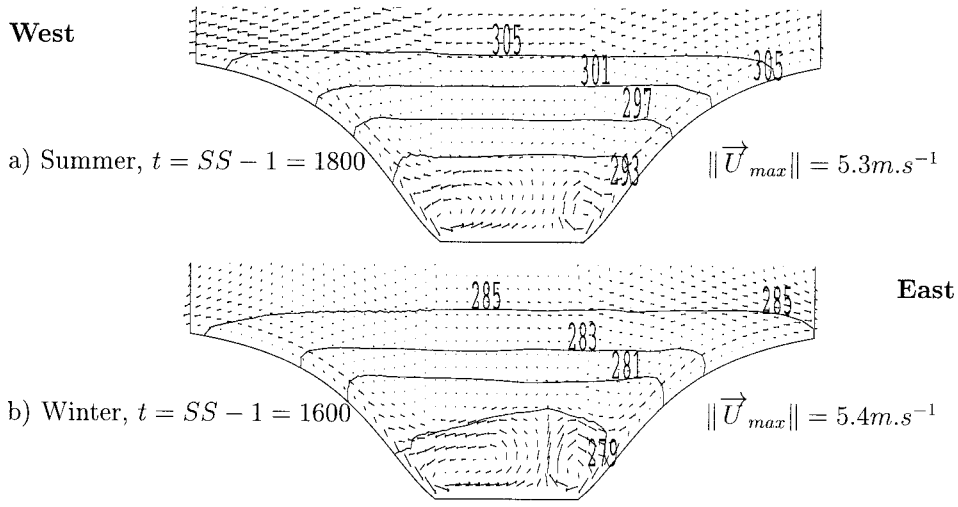

FIG. 10. Vertical cross section of the isovalue of the potential temperature Θ and the velocity vectors.

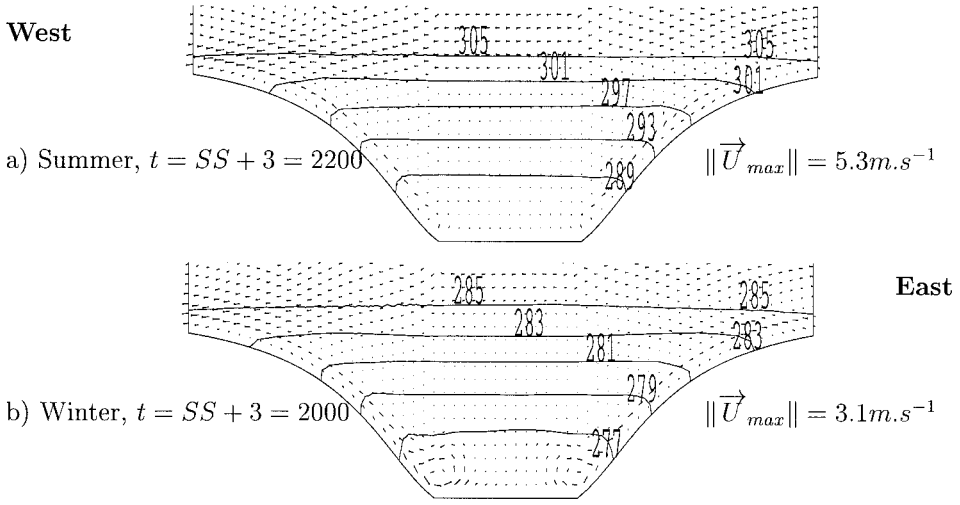

FIG. 11. Vertical cross section of the isovalue of the potential temperature Θ and the velocity vectors.

velocities is therefore drastically reduced within the valley.

c. *Breakup and formation of the temperature inversions*

As can be seen from the previous results, the velocity field is directly linked to the thermal structure of the atmosphere. Therefore, we now focus on the analysis of the vertical distribution of temperature and its evolution with time.

1) DETERMINATION OF THE CHARACTERISTIC LENGTH SCALES OF THE INVERSION LAYER

The characteristic length scale of the inversion layer within the valley is derived from the vertical potential temperature profile by calculating the altitudes of the base level z_i and the top level h_{st} of the inversion layer. A simple method has been developed to obtain these two altitudes from the second derivative of the potential temperature profile. Usually, the altitude of the top level z_i of the CBL, which also corresponds to the base level of the inversion layer, is defined to be the altitude where the heat flux $\widetilde{W\Theta}$ is minimum (mark 1 in Fig. 12). The correlation $\widetilde{W\Theta}$ is expressed with the resolved-scale variables W and Θ by

$$\widetilde{W\Theta} = (W - \overline{W}^y)(\Theta - \overline{\Theta}^y), \tag{10}$$

where the variable $\overline{\Psi}^y$ corresponds to the average of Ψ within the transverse direction y. This definition will be later referenced as M1.

As seen in Fig. 12, the altitude referenced by mark 1 is very similar to the one referenced with mark 2,

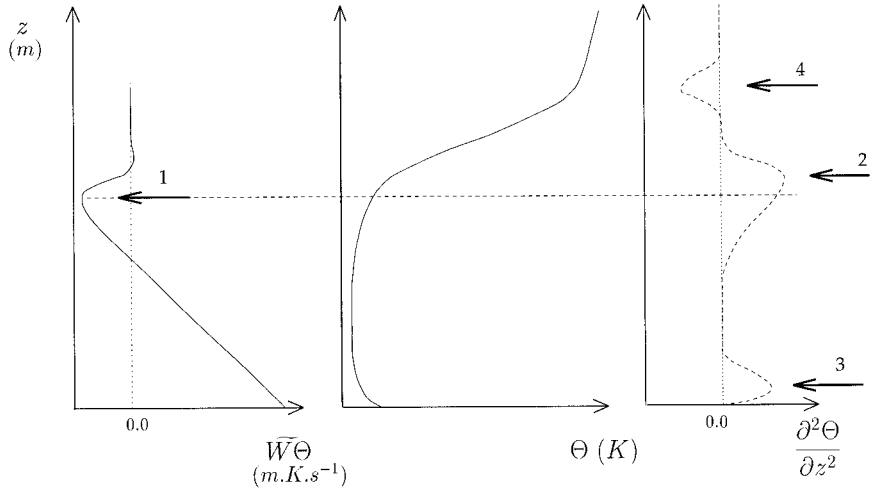

FIG. 12. Schematic representation of the vertical profile Θ within the CBL and its associated heat flux profile.

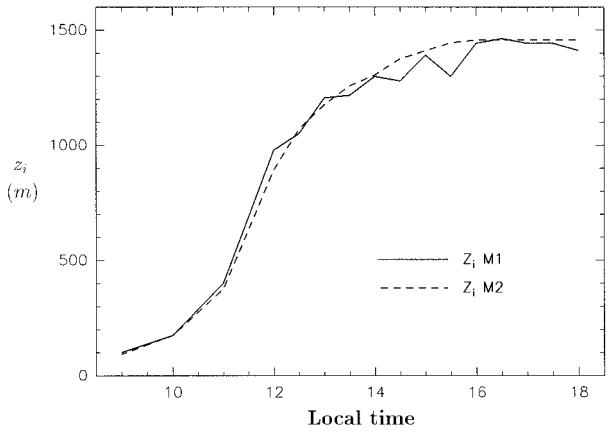

FIG. 13. Determination of the top level z_i of the CBL for day 33 of the Wangara experiment. Comparison between methods M1 and M2.

which was determined from the maximum of the second derivative of the potential temperature. Therefore, the instantaneous vertical profiles of the temperature are interpolated on a grid three times smaller than the calculated grid using a spline method. From this interpolated temperature vertical profile, the second derivative of the potential temperature profile is calculated. From this profile, the altitude h_{st} and z_i are obtained by h_{st} is the altitude where $\partial^2\langle\Theta\rangle/\partial z^2$ is minimum, while $\partial\langle\Theta\rangle/\partial z > 0$ (mark 4 in Fig. 12), and z_i is the altitude where $\partial^2\langle\Theta\rangle/\partial z^2$ is maximum, while $\partial\langle\Theta\rangle/\partial z > 0$ (mark 2 in Fig. 12).

Below the altitude z_i, the atmosphere is unstable and/or neutral and is called the convective boundary layer. Above the altitude h_{st}, the atmosphere is neutrally or slightly stably stratified. Between the altitudes z_i and h_{st}, the atmosphere is stably stratified and is called the inversion layer.

This method (later referenced by M2) has been validated by calculating the top level z_i of the CBL for day 33 of the Wangara experiment. In Fig. 13, the estimates of z_i using the two methods are plotted. As can be seen, the two methods give the same evolution with a smoother curve for M2 due to the highly variable heat flux compared to the vertical potential temperature profile. The method M2 is simpler and requires less CPU time and is therefore preferred over M1.

The instantaneous values of z_i and h_{st} have been averaged along the north–south and east–west directions only above the width of the valley at ridgetop level. Therefore, the values $z_{i,mean}$ and $h_{st,mean}$ (Fig. 14) characterize the structure of the evolution of the inversion layer within the valley core. To determine the valley side effect, we have also averaged in two different domains: $z_{i,east}$ from the east side to the middle of the valley and $z_{i,west}$ from the west side to the middle of the valley.

From Fig. 14a, note that the height of the convective layer z_i remains horizontal with time in the valley for the summer season. The curves $z_{i,east}$, $z_{i,mean}$, and $z_{i,west}$

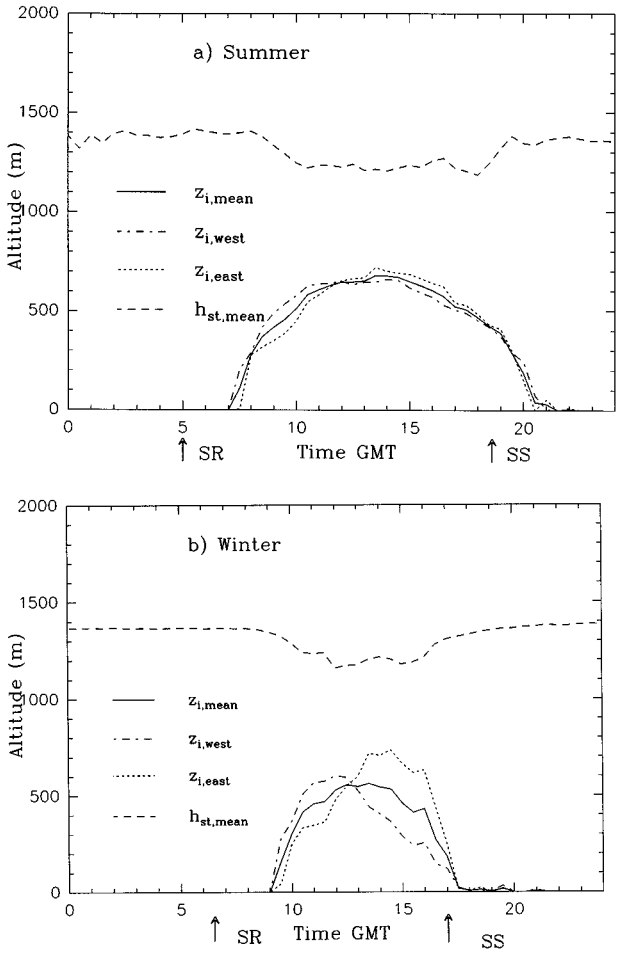

FIG. 14. Time evolution of the base level z_i and the top level h_{st} of the inversion layer.

collapse together in summer, whereas in winter (Fig. 14b), these curves show differences and involve a nonhorizontal height of the convective layer z_i. Therefore, one might conclude that the CBL within the valley leads to a more effective mixing in the lower layers of the atmosphere in summer. This point has been already observed by Whiteman (1982) and is the basis for the first pattern of inversion destruction. Moreover, Fig. 14 shows that the NIL altitude h_{st} seems to be independent of the season.

The choice for the simulation parameters (soil, initial stratification, valley geometry) does not allow the valley inversion to be completely destroyed. Bulk calculations of energy show that the available solar energy is significantly smaller than the energy required to destroyed the inversion layer. What may appear as an underestimation of energy forcing may be attributed to the initial ground temperature and the initial stratification. It may be attributed to either the soil model or the rather crude space resolution, which may cause trouble especially for the estimation of the fluxes near the ground. Nevertheless, the persistence of an inversion layer can be

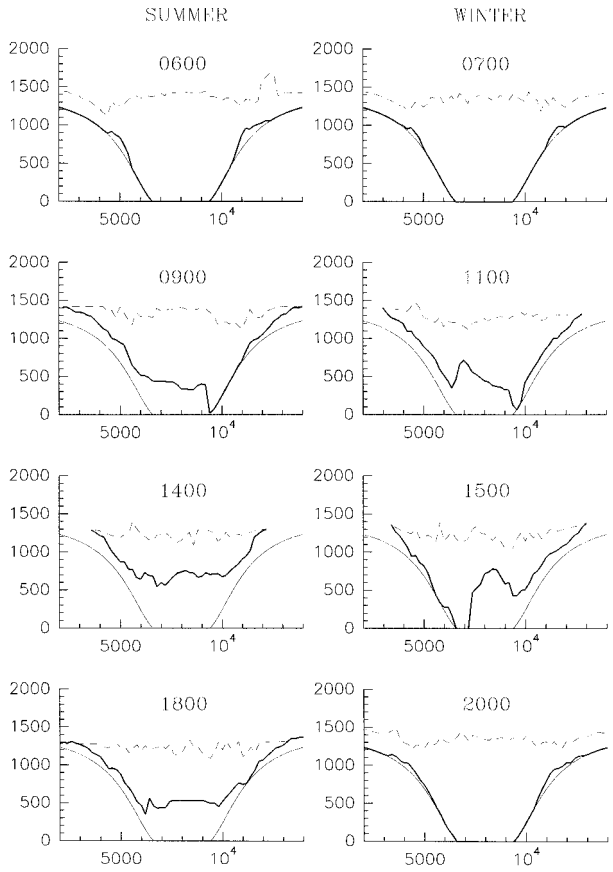

FIG. 15. Base level z_i and top level h_{st} of the inversion layer for both seasons: z_i (solid line) and h_{st} (dashed line).

observed over periods of several days. Therefore, a cold pool remains in the upper part of the valley, corresponding to the gap between the curves $z_{i,\text{mean}}$ and $h_{\text{st,mean}}$, even at the warmest time of the day (1400 LT) when the convective layer at the ground is most effective.

To add some spatial variability to the representation of the structure of the inversion layer, the instantaneous altitudes z_i and h_{st} averaged in the north–south direction have been drawn in Fig. 15 at the same times as that of Figs. 7–11. This representation shows the complex structure of the thermal field and its time evolution. In the summer, the horizontal variation of z_i is small across the valley, both during its growth and its depletion, throughout the day, whereas, in the winter, the position of the maximum value of z_i is directly related to the maximum solar exposure of the soil. The structure of the atmosphere consist of a series of layers with different characteristics (length scale, duration, etc.), which are analyzed below.

2) GROWTH OF THE CONVECTIVE BOUNDARY LAYER

The main timescales of the growth of the CBL are given in Table 3. The maximum vertical extent of the CBL (i.e., $z_{i,\text{mean}} \simeq 700$ m in summer and $z_{i,\text{mean}} \simeq 550$ m in winter) is obtained after $T_{\max} = 6$ h of growth in summer and $T_{\max} = 4$ h in winter. This parameter is considered instead of the destruction period of the inversion layer because of the nontotal destruction of the inversion layer. For practical use (i.e., pollutant dispersal within a deep valley), this parameter is more general since inversions may persist for several days, especially in winter. This time is in the range of the inversion breakup duration time observed by Whiteman (1982). The growth rate of the CBL ($\delta z_i/\delta t$) is slightly lower in summer than in winter, whereas the sensible flux is roughly twice the one in winter. As mentioned by Bader and McKee (1985), high initial stratification leads to a lower growth rate of the CBL because most of the sensible heat flux acts to reduce the initially strong lapse rate. In this study, the stratification in summer at dawn is found higher than in winter due to the initially imposed Brunt–Väisälä frequency. The CBL, $T_{\text{CBL,life}}$, lasts for 14 h in summer but only 7.5 h in winter. The important difference between the two seasons is directly related to the heat flux from the ground generated by the soil effect, and, in particular, to the solar radiation, which is more effective in summer than in winter. The magnitude of the sensible heating is probably the essential factor for the determination of characteristic timescale of the valley inversion breakup, as already mentioned by Bader and McKee (1985). Therefore, the duration of the CBL is approximately equivalent to the sunshine period (i.e., $T_{\text{SR}-\text{SS}}$) in summer, whereas in winter, the duration of the CBL corresponds to only about 70% of the sunshine period.

TABLE 3. Timescales (h) of the growth of the CBL.

	Summer	Winter
$T_{\max}$	6	4
$T_{\text{CBL,life}}$	14	7.5
$T_{\text{SR}-\text{SS}}$	13.75	10.5
Spatial structure	Symmetric	Time dependent

3) THE NOCTURNAL INVERSION LAYER

The characteristics of the NIL for both seasons are deduced from the average vertical potential temperature profile in Fig. 6. The duration of the NIL $T_{\text{NIL,life}}$ starts when the stratification becomes stable at the ground and stops when the first convective structure appears within the valley. The intensity of the inversion is given in terms of the Brunt–Väisälä frequency (N). These two quantities ($T_{\text{NIL,life}}$ and N) are summarized in Table 4.

TABLE 4. Characteristic scales of the NIL.

	Summer	Winter
$T_{\text{NIL,life}}$ (h)	10	15
Intensity N (s^{-1})	2.1×10^{-2}	1.5×10^{-2}

TABLE 5. Vertical extent of the NIL.

		h_{st}/H		
	H (m)	Summer		Winter
Present study	1260	1.11		1.09
Kuwagata and Kimura (1995)	1900	0.84	→	1.26

The vertical extent of the NIL (h_{st}) at the end of the night is on the order of the depth of the valley (H), as shown in Table 5. The parameter h_{st}/H is similar for both seasons in our study. The observations made by Kuwagata and Kimura (1995) give the same tendency.

4. Conclusions

The complete diurnal cycle of the formation and destruction of the valley inversion has been simulated with a 3D numerical model in an idealized quasi-2D valley for a dry atmosphere. The simulations have been run for two typical days—one in winter (February) and the other one in summer (August)—in order to show the influence of the season on the mechanism responsible for the valley inversion.

For this purpose, a 3D, nonhydrostatic atmospheric model (Submeso) has been developed on the basis of ARPS 3.1 (University of Oklahoma). This model includes several parameterizations that take into account all the physical processes playing a major role in our scale of interest (i.e., $L \simeq$ few kilometers and $T \simeq$ the diurnal cycle). The soil exchanges, which are the only forcing (through the solar radiation), are calculated from a two-layer model developed specifically for use at this scale. Moreover, the subgrid-scale closure has been chosen in order to take account of the space and time variability of the atmospheric stratification, as well as transport of the kinetic energy produced close to the ground surface toward the upper part of the atmosphere.

A simple method based on the analysis of the vertical potential temperature profile has been proposed to determine the characteristic height scales of the inversion (i.e., the height of the top of the CBL z_i, which is also the base of the inversion layer, and the inversion layer top h_{st}).

Due to the choice of the valley aspect ratio and the initial stratification, convective cells are able to develop at the ground. They reduce the direct effect of the slope winds on the dynamic structure within the valley.

The destruction of the NIL, for both seasons, corresponds to the third pattern of temperature structure evolution detailed by Whiteman (1982). Particularly noteworthy is the influence of the season on the structure of the CBL that develops from the ground due to solar warming. In summer, the altitude of the top of the CBL z_i remains approximately constant across the valley. The time evolution of the structure of the atmosphere is, therefore, close to the classic one described in textbooks (e.g., Stull 1988). On the other hand, in winter, this altitude varies with location within the valley. The dissymmetry of the thermal structure across the valley is especially marked at the beginning and end of the day. At 1200 LT, due to the maximum solar radiative flux, the thermal structure is close to the one in summer. In Fig. 14, the three curves describing winter conditions collapse together at 1200 LT. The vertical extent of the NIL seems to be less dependent on the season than on the nature of the ground and the valley geometry and is found to be roughly equal to the depth of the valley. Nevertheless, the duration of the inversion layer depends on the season. Due to the more effective solar radiation in summer, the inversion layer is present for a shorter time, leading to a more mixed atmospheric layer within the valley.

The formation and destruction of the NIL that typically fills a mountain valley has important implications for air pollution. Indeed, the inversion layer acts as a lid reducing drastically any vertical exchange. Therefore, any emitted pollutant can be trapped close to its emission location and high concentrations may build up. Therefore, a better comprehension and improved description of the dynamics of the atmosphere at valley scales can be useful for future urban planning for cities located in a mountainous area.

Acknowledgments. This work has been partly sponsored by the GdR C.N.R.S. 1102, Atmosphère Urbaine à Submeso Echelle. The numerical simulations were carried out on the Cray C98 of the IDRIS (CNRS) and on the Cray C94 of the CEA computing centers. Furthermore, the authors would like to thank the staff of the Center for Analysis and Prediction of Storms (CAPS, University of Oklahoma) and especially Dr. K. Droegemeier, its director, for his continuous help with the development of Submeso.

REFERENCES

André, J. C., P. Goutorbe, and A. Perrier, 1986: HAPEX-MOBILHY: A hydrologic atmospheric experiment for the study of water budget and evaporation flux at the climatic scale. *Bull. Amer. Meteor. Soc.*, **67,** 138–144.

Asselin, R. A., 1972: Frequency filter for time integration. *Mon. Wea. Rev.*, **100,** 487–490.

Bader, D. C., and T. B. McKee, 1983: Dynamical model simulation of the morning boundary layer development in deep mountain valleys. *J. Climate Appl. Meteor.*, **22,** 341–351.

——, and ——, 1985: Effects of shear, stability and valley characteristics on the destruction of temperature inversions. *J. Climate Appl. Meteor.*, **24,** 822–832.

Byun, D. W., 1990: On the analytical solutions of flux-profile relationships for the atmospheric surface layer. *J. Appl. Meteor.*, **29,** 652–657.

CAPS, 1993: ARPS Version 3.1 user's guide. CAPS, University of Oklahoma, Norman, OK, 183 pp. [Available from Center for Analysis and Prediction of Storms, University of Oklahoma, 100 E. Boyd St., Norman OK 73019.]

Clapp, R. B., and G. M. Hornberger, 1978: Empirical equations for some hydraulic properties. *Water Resour. Res.*, **14,** 601–604.

Clements, W. E., J. A. Archuleta, and P. H. Gudiksen, 1989: Exper-

imental design of the 1984 ASCOT Field Study. *J. Appl. Meteor.*, **28,** 405–413.

Deardorff, J. W., 1974: Three-dimensional numerical study of the height and mean structure of a heated planetary boundary layer. *Bound.-Layer Meteor.,* **7,** 81–106.

——, 1980: Stratocumulus-capped mixed layers derived from a three-dimensional model. *Bound.-Layer Meteor.*, **18,** 495–527.

Gal-Chen, T., and R. C. J. Somerville, 1975: On the use of the coordinate transformation for the solution of Navier–Stokes equations. *J. Comput. Phys.*, **17,** 209–228.

Garrett, A. J., 1983: Drainage flow prediction with a one-dimensional model including canopy, soil and radiation parametrizations. *J. Climate Appl. Meteor.*, **22,** 79–91.

Guilbaud, C., 1996: Etudes des inversions thermiques: Application aux écoulements atmosphériques dans des vallées encaissées. Ph.D. thesis, Université Joseph Fourier, Grenoble, France, 189 pp. [Available from LEGI, Université Joseph Fourier, B.P. 53, 38041 Grenoble Cedex 9, France.]

——, J. P. Chollet, and S. Anquetin, 1997: Large eddy simulations of stratified atmospheric flows within a deep valley. *Direct and Large Eddy Simulation II,* J.-P. Chollet, L. Kleiser, and P. Voke, Eds., ERCOFTAC Series, Vol. 5, Kluwer Academic, 157–166.

Heilman, W., and R. Dobosy, 1985: A nocturnal atmospheric drainage flow simulation investigating the application of one-dimensional modeling and current turbulence schemes. *J. Climate Appl. Meteor.*, **24,** 924–936.

Klemp, J. B., and D. K. Lilly, 1978: Numerical simulation of hydrostatic mountain waves. *J. Atmos. Sci.*, **35,** 78–107.

——, and R. B. Wilhelmson, 1978: The simulation of three-dimensional convective storm dynamics. *J. Atmos. Sci.*, **35,** 1070–1096.

Kuwagata, T., and F. Kimura, 1995: Daytime boundary layer evolution in a deep valley. Part I: Observations in the Ina Valley. *J. Appl. Meteor.*, **34,** 1082–1091.

Louis, J. F., 1979: A parametric model of vertical eddy fluxes in the atmosphere. *Bound.-Layer Meteor.*, **17,** 187–202.

Moeng, C. H., 1984: A large eddy simulation model for the study of planetary boundary layer turbulence. *J. Atmos. Sci.*, **41,** 2052–2062.

Noilhan, J., and S. Planton, 1989: A simple parameterization of land surface processes for meteorological models. *Mon. Wea. Rev.*, **117,** 536–549.

Oke, T. R., 1987: *Boundary Layer Climates.* 2d ed. Routledge, 435 pp.

Satomura, T., 1989: Compressible flow simulations on numerically generated grids. *J. Meteor. Soc. Japan,* **67,** 473–482.

Stull, R. B., 1988: *An Introduction to Boundary Layer Meteorology.* Kluwer Academic, 666 pp.

Tanguay, M., A. Robert, and R. Laprise, 1990: A semi-implicit semi-Lagrangian fully compressible regional forecast model. *Mon. Wea. Rev.*, **118,** 1970–1980.

Whiteman, C. D., 1982: Breakup of temperature inversions in deep mountain valleys: Part I. Observations. *J. Appl. Meteor.*, **21,** 270–289.

——, T. B. McKee, and J. C. Doran, 1996: Boundary layer evolution within a canyonland basin. Part I: Mass, heat, and moisture budgets from observations. *J. Appl. Meteor.*, **35,** 2145–2161.

Wong, R. K. W., K. D. Hage, and L. D. Philips, 1987: The numerical simulation of drainage winds in a small urban valley under conditions with supercritical Richardson number. *J. Climate Appl. Meteor.*, **26,** 1447–1463.

Xue, M., K. K. Droegemeier, V. Wong, A. Shapiro, and K. Brewster, 1995: ARPS Version 4.0 user's guide. CAPS, University of Oklahoma, Norman, OK, 380 pp. [Available from Center for Analysis and Prediction of Storms, University of Oklahoma, 100 E. Boyd St., Norman, OK 73019.]

Yamada, T., and G. Mellor, 1975: A simulation of the Wangara atmospheric boundary layer data. *J. Atmos. Sci.*, **32,** 2309–2329.